Three-dimensional modeling of equatorial spread F airglow enhancements

J. Krall,[1] J. D. Huba,[2] and C. R. Martinis[2]

Received 7 April 2009; accepted 30 April 2009; published 22 May 2009.

[1] A sequence of 630.0 nm images obtained with the Boston University all-sky imaging system at Arecibo (18.3 N, 66.7 W, 28 N mag) shows equatorial spread F (ESF) airglow depletions evolving into ESF airglow enhancements. Using a combination of a meridional wind and a converging zonal wind, the NRL ionosphere model SAMI3/ESF can reproduce ESF airglow enhancements. **Citation:** Krall, J., J. D. Huba, and C. R. Martinis (2009), Three-dimensional modeling of equatorial spread F airglow enhancements, *Geophys. Res. Lett.*, *36*, L10103, doi:10.1029/2009GL038441.

1. Introduction

[2] Equatorial spread F (ESF) is the formation, growth, and upward motion of plasma depletions in the low latitude ionosphere [*Kelley*, 1989; *Sultan*, 1996; *Eccles*, 1998]. ESF is an important component of space weather because it can disrupt global communication and navigation systems [*de La Beaujardiere et al.*, 2004; *Steenburgh et al.*, 2008] and is the subject of many ongoing research programs worldwide.

[3] A rare and unexplained phenomenon related to airglow signatures of ESF plumes has been observed at Arecibo [*Martinis et al.*, 2009; *Seker et al.*, 2007; C. Martinis et al., Imaging studies of ionospheric irregularities, paper presented at CEDAR Workshop, National Science Foundation, Santa Fe, New Mexico, 2006]. Occasionally, near the northern winter solstice, ESF airglow depletions evolve into bright structures called "ESF airglow enhancements." An example of these airglow structures, which are described in greater detail by *Martinis et al.* [2009], is shown in Figure 1. These 630.0 nm images were recorded by the Boston University All-Sky Imager (ASI) at Arecibo (18.3°N, 66.7°W, 28°N Mag) on 26 December 2003, 0202-0514 UT ($\simeq$2202-0114 LT). These are unwarped images assuming an emission height of 300 km. In the ASI images, a large airglow depletion associated with ESF first moves upward in latitude while slowly moving eastward (frames 1 and 2), then appears to fill in from the sides (frame 3), and finally fills in entirely, becoming brighter/denser, while moving slowly westward (frame 4). In addition, what appears to be a second depletion associated with ESF is seen to the south (frames 1 and 2), grows (frame 3), and begins moving westward (frame 4).

[4] In this letter, we consider the hypothesis that neutral winds are responsible for these phenomena. We find that with a combination of a meridional wind and a converging zonal wind, SAMI3/ESF simulations [*Huba et al.*, 2008] can reproduce ESF airglow enhancements. The key phenomena underlying this result are 1) a steady, mild, meridional wind (20 m/s) in combination with the super fountain effect of *Huba et al.* [2009] can cause a density enhancement in the downwind "leg" of the field-aligned ESF plume at altitudes of 400–1000 km and 2) a converging zonal wind can affect the ESF plume in such a way that upward $\mathbf{E} \times \mathbf{B}$ drifts cease, allowing this enhanced density to fall to a height ($\sim$300 km) where it can contribute to airglow. Converging zonal winds are commonly observed at night [*Wharton et al.*, 1984; *Herrero et al.*, 1985], when typically-eastward dusk winds transition to typically-westward dawn winds. The observed depletions in this case halt their eastward drift before transitioning from dark to light, which suggests that they are co-located with the converging winds.

2. Numerical Model

[5] We have recently developed a version of the NRL SAMI3 ionospheric simulation code [*Huba et al.*, 2000, 2005], SAMI3/ESF, that simulates a "wedge" of the post-sunset ionosphere [*Huba et al.*, 2008]. The SAMI3/ESF potential equation is derived from current conservation ($\nabla \cdot \mathbf{J} = 0$) in dipole coordinates (s, p, ϕ). The equation used in this study is

$$\frac{\partial}{\partial p} p \Sigma_{pp} \frac{\partial \Phi}{\partial p} - \frac{\partial}{\partial p} \Sigma_H \frac{\partial \Phi}{\partial \phi} + \frac{\partial}{\partial \phi} \frac{1}{p} \Sigma_{p\phi} \frac{\partial \Phi}{\partial \phi} + \frac{\partial}{\partial \phi} \Sigma_H \frac{\partial \Phi}{\partial p} = \frac{\partial F_{\phi g}}{\partial \phi} + \frac{\partial F_{\phi V}}{\partial \phi} + \frac{\partial F_{pg}}{\partial p} + \frac{\partial F_{pV}}{\partial p} \quad (1)$$

where $F_{\phi g} = \int (r_E \sin^3\theta/\Delta)\,(B_0/c)\sigma_{Hc} g_p\, ds$, $F_{\phi V} = \int (r_E \sin^3\theta/\Delta)\,(B_0/c)\,(\sigma_H V_{n\phi} - \sigma_P V_{np})\, ds$, $F_{pg} = -\int r_E \sin\theta (B_0/c) \sigma_{Pc} g_p\, ds$, and $F_{pV} = \int r_E \sin\theta (B_0/c)\,(\sigma_P V_{n\phi} + \sigma_H V_{np})\, ds$. Here Φ is the potential, g_p is the component of gravity perpendicular to $\mathbf{B}$, V_{np} and $V_{n\phi}$ are perpendicular wind components, σ_P is the Pedersen conductivity, σ_H is the Hall conductivity,

$$\sigma_{Pc} = \sum_i \frac{n_i ec}{B\Omega_i} \frac{\nu_{in}/\Omega_i}{1 + \nu_{in}^2/\Omega_i^2} \quad (2)$$

and

$$\sigma_{Hc} = \sum_i \frac{n_i ec}{B\Omega_i} \frac{1}{1 + \nu_{in}^2/\Omega_i^2} \quad (3)$$

are the ion components of the Pedersen and Hall conductivities, respectively, each divided by the ion cyclotron frequency, $\Sigma_{pp} = \int (p\Delta/b_s)\sigma_P\, ds$, $\Sigma_{p\phi} = \int (1/$

[1] Plasma Physics Division, Naval Research Laboratory, Washington, D. C., USA.

[2] Center for Space Physics, Boston University, Boston, Massachusetts, USA.

0094-8276/09/2009GL038441$05.00

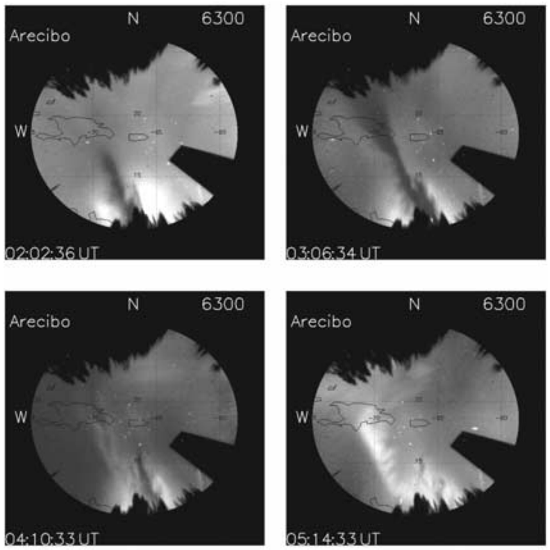

Figure 1. A sequence of 630.0 nm unwarped images obtained with the Boston University ASI at Arecibo on 26 December 2003. Grid lines are at 5° intervals. Obstructions by trees occur on the north and south horizons, with a light-blocking mask in the southeast.

$pb_s\Delta)\sigma_P\, ds$, $\Sigma_H = \int \sigma_H/b_s\, ds$, $\Delta = (1 + 3\cos^2\theta)^{1/2}$, $\Omega_i = eB/m_i c$ and $\Omega_e = eB/m_e c$ are cyclotron frequencies, ν_{in} and ν_{en} are collision frequencies, B is the local geomagnetic field, B_0 is the geomagnetic field at the equator, θ is the latitude, $b_s = (r_E^3/r^3)\Delta$, r_E is the radius of the earth, and field-line integrations with respect to coordinate s are along the entire flux-tube, with the base of the field lines being at 85 km.

3. Simulation of ESF Airglow

[6] As configured for this study, SAMI3/ESF is limited to 4 degrees in longitude with periodic boundary conditions. For simplicity SAMI3/ESF uses a non-tilted dipole field, so magnetic latitude and geographic latitude are the same, and the geographic longitude is set to 0°, so universal time and local time are the same. The geophysical parameters for these runs are similar to those of *Huba et al.* [2008] and *Krall et al.* [2009]: F10.7 = 170, F10.7A = 170, Ap = 4 and day-of-year 355. An ESF plume is seeded by imposing a Gaussian-like perturbation in the ion density at $t = 0$: a peak ion density perturbation of 5% centered at longitude 0 and altitude $z = 400$ km. We include a 20 m/s meridional wind and a converging zonal wind, which ramps up smoothly from zero on the west and east boundaries to ±10 m/s at the center. The simplified zonal wind is also a function of time, ramping up from zero to full speed during 2200-2400 UT.

[7] Results from this run are shown in Figures 2 and 3. As a proxy for the ASI images we first show contours of electron density versus longitude and latitude at a constant altitude of 288 km in Figure 2. Corresponding contour plots of $\log_{10} n_e$ in the magnetic equatorial plane are shown in Figure 3. The latitude range of Figure 2 (16–28°N Magnetic) is close to that of the Arecibo images (Figure 1). The altitude 288 km is used because it lies in the 630.0 nm airglow altitude range (250–300 km). As the simulated ESF depletion increases in height, it extends northward (and southward) in latitude, entering the field of view of Figure 2. At around 0200 UT, the ESF depletion in Figure 2 begins to "fill in." The ESF structure then brightens relative to the background (A). The second ESF depletion enters our field of view at this time (B).

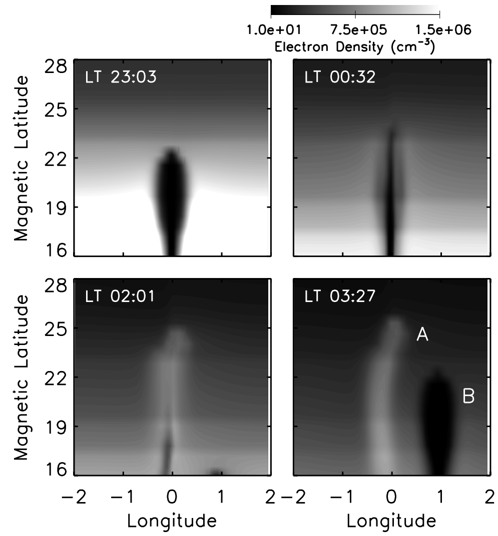

Figure 2. Electron density versus longitude and latitude at a constant altitude of 288 km from SAMI3/ESF. The latitude range lies in the northern half of the simulation.

[8] Comparing the model result in Figure 2 to the ASI images in Figure 1 we note that the ESF bubble first moves upward in latitude (frames 1 and 2), then fills in at the sides (frame 3), and finally fills in entirely, becoming brighter/denser (frame 4). In addition, a new ESF bubble comes into the field of view at later times (model frame 4; Arecibo frames 2 and 3). We note key differences between the model and the observation: the time scale is different (4.5 hours in the model versus 3.2 hours in the observations), the model ESF bubble does not extend as far in latitude as the observed bubble (25 versus 30°N Mag), and the fields of

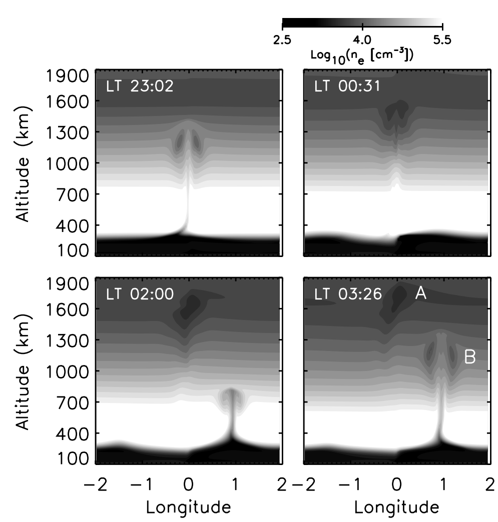

Figure 3. Contours of $\log_{10}(n_e)$ versus height and longitude at the magnetic equator at times corresponding to those in Figure 2.

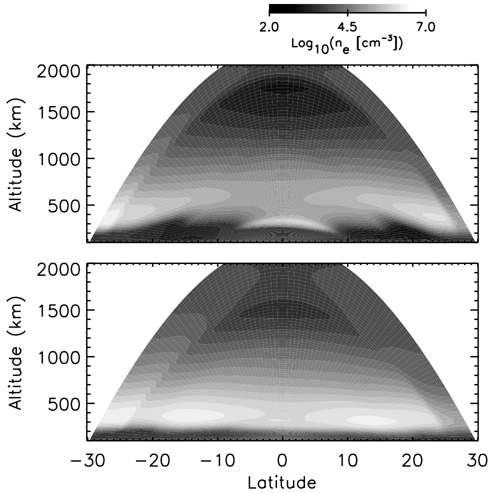

Figure 4. Contours of $\log_{10}(n_e)$ within the ESF bubble at 0330 UT plotted versus magnetic latitude and altitude for the case (top) with no zonal winds and (bottom) with converging zonal winds. A 20 m/s northward meridional wind is included in both simulations.

view have different widths (4° in the model versus 12° in the observations). Nevertheless, the similarities strongly suggest that a mechanism for ESF airglow enhancements is wind-driven. We note that the corresponding density plot at southern latitudes (not shown) does not show ESF airglow enhancement.

[9] A more conventional view of the result of Figure 2 is shown in Figure 3. Here contours of $\log_{10}n_e$ are plotted as a function of longitude versus altitude in the magnetic equatorial plane at the same times as the four frames of Figure 2. We first see the growth of the initially-seeded ESF plume at longitude −0.1° (frames 1 and 2). The converging zonal wind has the effect of weakening the ESF **E** field so that **E** × **B** drift velocities (not shown) fall rapidly after 2300 UT and the upward motion of the bubble is nearly halted (A). The wind also interacts with the *F* layer so as to seed another ESF bubble late in the simulation (B).

4. Simulation of an ESF Density Enhancement

[10] To further elucidate the airglow result of Figure 2, we present a SAMI3/ESF run with a 20 m/s meridional wind but with no zonal wind. In Figure 4 (top) we show contours of $\log_{10}n_e$ versus magnetic latitude and altitude at longitude −0.1° within the ESF plume at 0330 UT. The plume has apex height 1900 km; its extent is indicated by the discontinuity in the electron density at its outer edge. Prior to this time, strong **E** × **B** drifts within the plume drive a "super fountain effect" [*Huba et al.*, 2009], raising the height of the ionization anomaly within the bubble relative to the background.

[11] The meridional wind acts on this overall configuration, affecting both the background ionosphere and the plasma within the bubble. In the background, the southern ionization crest is lifted upwards along the field while the northern crest is pushed downwards. As a result, recombination in the northern crest becomes strong enough to overwhelm the density contribution of wind-driven transport of plasma from south to north. Within the ESF plume, strong **E** fields lead to ionization crests at a higher altitude than the background; these are not affected as strongly by recombination. As a result, transport and recombination are largely balanced within the plume and the south–north configuration is nearly symmetric. The net result is shown in Figure 4 (top), where the density at the outer edge of the northern leg clearly exceeds the background density over the altitude range 400–1000 km; this represents an ESF density enhancement.

[12] Figure 5 provides another diagnostic of the simulated ESF density enhancement, showing plots of the electron density versus longitude in the northern leg of the bubble (700 km, 22°N, solid curves) and at the conjugate point (dashed curves). These plots confirm that the meridional wind affects the background more strongly than the interior of the ESF plume. The ESF density enhancement shown here is similar to enhanced densities found in ROCSAT satellite measurements at altitude 570 km [*Martinis et al.*, 2009] and to those found in ROCSAT and DMSP satellite data at 600 km and 850 km, respectively [*Le et al.*, 2003], with moderate drifts (usually upward in comparison to the background) and field-aligned flows (usually poleward).

[13] Despite the presence of ESF density enhancements at 400–1000 km, the run with no zonal wind does not reproduce the airglow result of Figure 2. This can be seen in Figure 4, where the uplift of the *F* layer within the bubble, evident at altitude 300 km in Figure 4 (top, no zonal winds), is absent in Figure 4 (bottom, with zonal winds). The key difference between Figures 4 (top) and 4 (bottom) is the disruption of the initial ESF plume by the zonal winds in Figure 4 (bottom). Introduction of the zonal wind leads to a severe reduction in the upward **E** × **B** drifts in that case; they fall by nearly two orders of magnitude between 2300 and 0100 UT. The cessation of upward **E** × **B** drifts allows the ESF density enhancement of Figure 5 to fall to lower

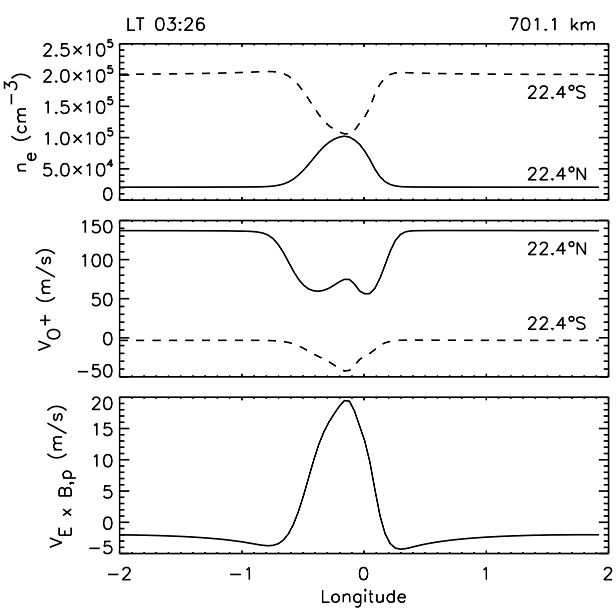

Figure 5. Plots of (top) n_e, (middle) field-aligned O^+ velocity (positive = northward), and (bottom) vertical **E** × **B** velocity versus longitude at fixed altitude 700 km and magnetic latitude 22.4°N. Dashed lines are at the conjugate point, 22.4°S.

altitude, filling in the ESF depletion at heights where airglow is generated.

5. Conclusions

[14] In this letter, we report the observation of the evolution of ESF airglow depletions into enhancements. We can reproduce ESF airglow enhancements with the NRL ionosphere model SAMI3/ESF [*Huba et al.*, 2008] using a combination of a meridional wind and a converging zonal wind. Here, a mild meridional wind (e.g., 20 m/s) transports plasma from south to north while pushing the northern ionization crest downward, enhancing recombination. This leads to asymmetric south–north electron density profiles both inside and outside of the ESF plume with the net effect being a density enhancement at altitudes of 400–1000 km in the northern (downwind) "leg" of the ESF plume. The introduction of a mild converging zonal wind (e.g., 10 m/s) disrupts the upward $\mathbf{E} \times \mathbf{B}$ drifts within the ESF plume, allowing the enhanced electron density to fall to the lower altitudes where airglow occurs and leading to the simulated ESF airglow enhancement.

[15] Our finding, that a converging zonal wind can disrupt ESF, deserves further study. Indeed, it is not yet clear whether the zonal winds are directly affecting the $\mathbf{E} \times \mathbf{B}$ drifts or if it is the potential associated with the second bubble ("B") that is responsible. A question of some interest has been, "what makes an ESF bubble stop rising?" One answer to this question is based on buoyancy considerations. Early papers on this subject [*Ott*, 1978; *Ossakow and Chaturvedi*, 1978] suggested that the bubble stops when the density of the plasma bubble equals the density of the background plasma. *Mendillo et al.* [2005] argued in favor of a balance between field-line integrated densities to better explain the observation of high altitude bubbles. Our result shows that ESF driving terms, which are quickly reduced when the $\mathbf{E} \times \mathbf{B}$ drift pattern is somehow interrupted, are also significant, perhaps more so than buoyancy forces.

[16] **Acknowledgments.** This work was supported by the Office of Naval Research and NASA. We thank Joel Fedder for a critical reading of the manuscript. C.M. acknowledges the support of NSF and ONR.

References

de La Beaujardiere, O., L. Jeong, and The C/NOFS Science Definition Teams (2004), C/NOFS: A mission to forecast scintillations, *J. Atmos. Sol. Terr. Phys.*, *66*, 1573–1591.

Eccles, J. V. (1998), Modeling investigation of the evening prereversal enhancement of the zonal electric field in the equatorial ionosphere, *J. Geophys. Res.*, *103*, 26,709–26,719.

Herrero, F. A., H. G. Mayr, N. W. Spencer, and A. E. Hedin (1985), Interaction of zonal winds with the equatorial midnight pressure bulge in the Earth's thermosphere: Check of momentum balance, *Geophys. Res. Lett.*, *12*, 491–494.

Huba, J. D., G. Joyce, and J. A. Fedder (2000), Sami2 is Another Model of the Ionosphere (SAMI2): A new low-latitude ionosphere model, *J. Geophys. Res.*, *105*, 23,035–23,053.

Huba, J. D., G. Joyce, S. Sazykin, R. Wolf, and R. Shapiro (2005), Simulation study of penetration electric fields in the low- to mid-latitude ionosphere, *Geophys. Res. Lett.*, *32*, L23101, doi:10.1029/2005GL024162.

Huba, J. D., G. Joyce, and J. Krall (2008), Three-dimensional equatorial spread *F* modeling, *Geophys. Res. Lett.*, *35*, L10102, doi:10.1029/2008GL033509.

Huba, J. D., J. Krall, and G. Joyce (2009), Atomic and molecular ion dynamics during equatorial spread *F*, *Geophys. Res. Lett.*, doi:10.1029/2009GL037675, in press.

Kelley, M. C. (1989), *The Earth's Ionosphere, Plasma Physics and Electrodynamics*, Academic, San Diego, Calif.

Krall, J., J. D. Huba, G. Joyce, and S. T. Zalesak (2009), Three-dimensional simulation of equatorial spread-*F* with meridional wind effects, *Ann. Geophys.*, in press.

Le, G., C.-S. Huang, R. F. Pfaff, S.-Y. Su, H.-C. Yeh, R. A. Heelis, F. J. Rich, and M. Hairston (2003), Plasma density enhancements associated with equatorial spread *F*: ROCSAT-1 and DMSP observations, *J. Geophys. Res.*, *108*(A8), 1318, doi:10.1029/2002JA009592.

Martinis, C., J. Baumgardner, M. Mendillo, and S.-Y. Su (2009), Brightening of 630.0 nm airglow depletions observed at midlatitudes, *J. Geophys. Res.*, doi:10.1029/2008JA013931, in press.

Mendillo, M., E. Zesta, S. Shodham, P. J. Sultan, R. Doe, Y. Sahai, and J. Baumgardner (2005), Observations and modeling of the coupled latitude-altitude patterns of equatorial plasma depletions, *J. Geophys. Res.*, *110*, A09303, doi:10.1029/2005JA011157.

Ossakow, S. L., and P. K. Chaturvedi (1978), Morphological studies of rising equatorial spread *F* bubbles, *J. Geophys. Res.*, *83*, 2085–2090.

Ott, E. (1978), Theory of rayleigh-taylor bubbles in the equatorial ionosphere, *J. Geophys. Res.*, *83*, 2066–2070.

Seker, I., J. Mathews, J. Wiig, P. Gutierrez, J. Friedman, and C. Tepley (2007), First results from the Penn State allsky imager at the Arecibo Observatory, *Earth Planets Space*, *59*, 165–176.

Steenburgh, R. A., C. G. Smithtro, and K. M. Groves (2008), Ionospheric scintillation effects on single frequency GPS, *Space Weather*, *6*, S04D02, doi:10.1029/2007SW000340.

Sultan, P. J. (1996), Linear theory and modeling of the Rayleigh-Taylor instability leading to the occurrence of equatorial spread *F*, *J. Geophys. Res.*, *101*, 26,875–26,891.

Wharton, L. E., N. W. Spencer, and H. G. Mayr (1984), The Earth's thermospheric superrotation from Dynamics Explorer 2, *Geophys. Res. Lett.*, *11*, 531–533.

J. D. Huba and J. Krall, Naval Research Laboratory, Code 6790, 4555 Overlook Avenue, S.W., Washington, DC, 20375–5000, USA. (jonathan.krall@nrl.navy.mil)

C. R. Martinis, Center for Space Physics, Boston University, 725 Commonwealth Avenue, Boston, MA 02215, USA.